Journal of
Materials Chemistry C

ROYAL SOCIETY
OF CHEMISTRY

PAPER

View Article Online
View Journal | View Issue

Check for updates

Cite this: *J. Mater. Chem. C*, 2023, **11**, 5515

Highly efficient broadband NIR phosphor $Y_2CaHfScAl_3O_{12}$:Cr^{3+},Yb^{3+} with superior thermal stability for spectroscopy applications†

Pengcheng Luo,[ab] Dashuai Sun,*[b] Zeyu Lyu,[b] Sida Shen,[b] Zheng Lu,[b] Zhijun Li,[ab] Zhihang Yue,[b] Chengliang Lyu[b] and Hongpeng You *[abc]

Received 20th February 2023,
Accepted 28th March 2023

DOI: 10.1039/d3tc00634d

rsc.li/materials-c

The rising demand for spectroscopy applications in the fields of information encryption, non-invasive detection and component analysis has attracted extensive attention to achieve high power near-infrared (NIR) light sources. Near-infrared phosphor-converted light emitting diodes (NIR pc-LEDs) are regarded as ideal light sources to meet the current needs due to their advantages of high power, low cost, and portability. However, it remains a huge challenge to design a NIR phosphor with high emission efficiency, superior thermal stability, and broadband emission. Herein, a novel NIR phosphor, $Y_2CaHfScAl_3O_{12}$:Cr^{3+} (YCHSA:Cr^{3+}), is reported from a fundamental study of garnet type inorganic materials. YCHSA:Cr^{3+} displays an intense broadband NIR emission covering from 650 to 900 nm with a full width at half maximum (FWHM) of 110 nm and good thermal stability ($I_{423K/303K}$ = 76%). Furthermore, we reasonably utilized the energy transfer from the Cr^{3+} to Yb^{3+} ions and obtained the YCHSA:0.08Cr^{3+},0.03Yb^{3+} phosphor, and achieved performance improvement with a broader NIR emission band (FWHM = 327 nm) as well as better thermal stability (up to $I_{423K/303K}$ = 83%). The excellent performance of NIR pc-LED is crucial for spectroscopy applications. The optimal samples and 450 nm commercial blue chips are packaged into NIR pc-LEDs, and give a high output power of 63.6 mW at a drive current of 100 mA. Finally, the superior performance in information encryption and non-invasive detection is demonstrated.

Introduction

NIR light sources have been widely applied in various fields, such as information encryption, non-invasive detection, component analysis, night vision, and plant growth illumination.[1,2] As the traditional NIR light sources, incandescent lamps are shelved due to their low energy conversion efficiency, large size, and short lifetime. AlGaAs LEDs are attractive NIR light sources due to their high efficiency and small size. However, the high cost and narrow NIR emission band (FWHM $\leq$ 50 nm) impose roadblocks in promoting their application.[3,4] Recently, NIR pc-LEDs as a new generation of NIR light sources have drawn extensive attention. NIR pc-LEDs have many superior properties such as small size, broadband emission, high efficiency, and excellent thermal stability. The compactness facilitates the widespread use of NIR light sources. The broader NIR emission band ensures to expand the detection range, enabling the detection of components by using various responses of organic groups in the component analysis. The higher emission intensity in the long wavelength region (>1000 nm) contributes to greater biological tissue penetration in the field of non-invasive detection. The high efficiency not only saves energy but also reduces heat release, and the excellent thermal stability allows pc-LEDs to maintain good performance at operating temperatures.[5,6] These advantages depend on the excellent performance of the phosphors, as they are the ones that absorb the narrowband blue light of the chip and efficiently convert it to the desired NIR light.[7]

Over the past few years, many efforts have been made in the research of various activator doped NIR phosphors, such as $MgAl_2O_4$:Mn^{2+},[8] $Ba_3Lu(BO_3)_3$:Eu^{2+},[9] $K_3LuSi_2O_7$:Eu^{2+},[10] $Y_2Ti_2O_7$:Bi^{3+},[11] $Ca_3Y_2Ge_3O_{12}$:Cr^{3+},[12] $LiInSi_2O_6$:Cr^{3+},[13] and $Y_3In_2Ga_3O_{12}$:Cr^{3+}.[14] Unfortunately, the FWHM of all these NIR phosphor emission bands is less than 200 nm and the emission is weak at positions greater than 900 nm, limiting their application in many fields. To obtain super broadband NIR emission, researchers developed Cr^{3+}-doped phosphors with two or more different octahedral lattice sites, for example, $La_3Ga_5GeO_{14}$:Cr^{3+},[15] La_2MgZrO_6:Cr^{3+},[16] and Li_2MgZrO_4:Cr^{3+}.[17] However, the thermal stability of these phosphors is

---

[a] *School of Chemistry and Chemical Engineering, Nanchang University, Nanchang 330031, P. R. China. E-mail: hpyou@ciac.ac.cn*
[b] *Ganjiang Innovation Academy, Chinese Academy of Sciences, Ganzhou 341000, P. R. China. E-mail: dssun@gia.cas.cn*
[c] *State Key Laboratory of Rare Earth Resource Utilization, Changchun Institute of Applied Chemistry, Chinese Academy of Sciences, Changchun 130022, P. R. China*

† Electronic supplementary information (ESI) available. See DOI: https://doi.org/10.1039/d3tc00634d

poor, due to the fast non-radiative relaxation of the loosely coordinated Cr^{3+}. Another strategy is to introduce Yb^{3+} ions into Cr^{3+}-doped NIR phosphors to obtain super broadband NIR phosphors by constructing the energy transfer from Cr^{3+} to Yb^{3+} ions, such as $Ca_4ZrGe_3O_{12}$:Cr^{3+},Yb^{3+},[18] $LiScP_2O_7$:Cr^{3+},Yb^{3+},[19] and $Lu_2CaMg_2Ge_3O_{12}$:Cr^{3+},Yb^{3+}.[20] but they also suffer from low quantum yield (QY) and/or poor thermal stability. Therefore, it is of great theoretical and practical value to actively explore new efficient super broadband and thermally stable NIR phosphors.

In this paper, we report a garnet-type YCHSA:0.08Cr^{3+} phosphor with broadband NIR emission (FWHM = 110 nm) and good thermal stability ($I_{423K/303K}$ = 76%). Furthermore, introducing Yb^{3+} ions into YCHSA:0.08Cr^{3+} led to a broader emission band (FWHM = 327 nm) and better thermal stability ($I_{423K/303K}$ = 83%). The optimized NIR pc-LED is fabricated by combining YCHSA:0.08Cr^{3+},0.03Yb^{3+} with a commercial blue LED chip, giving a high output power of 63.6 mW at a drive current of 100 mA, and its applications in information encryption and non-invasive detection are demonstrated.

Experimental section

Material synthesis.

Typically, YCHSA:Cr^{3+},Yb^{3+} phosphors were synthesized by a high-temperature solid-state reaction method. According to the $Y_2CaHfScAl_3O_{12}$:$x$$Cr^{3+}$,$y$$Yb^{3+}$ (x = 0.02 to 0.34, y = 0.01 to 0.16), the stoichiometric amounts of raw materials Y_2O_3 (99.999%), $CaCO_3$ (99%), HfO_2 (99.9%), Sc_2O_3 (99.99%), Al_2O_3 (99.99%), Cr_2O_3 (99%), and Yb_2O_3 (99.99%) were weighed and well-ground in agate for about 0.5 hours for full mixing. Then the mixture was transferred into covered corundum crucibles and pre-fired at 800 °C for 2 hours and finally sintered at 1550 °C for 4 hours under a reductive atmosphere (90% N_2 + 10% H_2). After being cooled down to room temperature, the final products were ground to obtain the target green powders.

Characterization

Powder X-ray diffraction (XRD) measurements were performed on a D8 Advance Power Diffractometer (Bruker Corporation, Germany) at 40 kV and 40 mA with Cu Kα radiation (λ = 1.5406 Å). The Rietveld refinement was performed using the FullProf program. Diffuse reflection spectra (DRS) of samples were recorded using a UV-vis-NIR spectrometer (Hitachi UH4150). The particle morphology and energy dispersive X-ray (EDS) mapping of samples were characterized by scanning electron microscopy (SEM, JSM-IT800) equipped with an EDS detector (Oxford Aztec Standard X-MaxN 100 mm^2). Photoluminescence excitation spectra, photoluminescence spectra and temperature-dependent (303–483 K) spectra were recorded using an Everfine EX-1000 Exciting Spectra And Thermal Quenching Analyzer For Phosphors. For the PL QY measurement, the samples were put inside an optical integrating sphere coupled to an Edinburgh Instruments FLS 980 spectrometer. The low temperature photoluminescence excitation spectra and photoluminescence spectra were recorded using an Edinburgh Instruments FLS-1000 spectrometer (Edinburgh Instruments, Edinburgh, UK). The fluorescence decay curves were measured using a fluorescence spectrophotometer (Edinburgh FLS1000). The NIR pc-LED devices were fabricated by mixing phosphor and transparent silicone resin at 1 : 1 and coating the 450 nm InGaN blue chips. The photoelectric properties of the pc-LEDs were measured using an integrating sphere spectroradiometer system (HASS-2000, 350–1650 nm, Everfine).

Results and discussion

Phase identification and crystal structure analysis

Fig. 1a shows the representative XRD patterns of undoped YCHSA, YCHSA:0.03Cr^{3+}, YCHSA:0.08Cr^{3+}, and YCHSA:0.08Cr^{3+},0.03Yb^{3+} samples, and standard cards of $Ca_2GdZr_2Al_3O_{12}$ (COD-4338781). One can see that the XRD peaks of the samples match well with the diffraction peaks of the standard cards, indicating that we have successfully synthesized the samples. There are minor diffraction peaks from $CaHfO_3$ (PDF#36-1473) impurities. Due to their very small amount, the effect of $CaHfO_3$ on photoluminescent properties of YCHSA:Cr^{3+},Yb^{3+} can be ignored. Fig. 1b shows the crystal structure of YCHSA. It is composed of [YO_8/CaO_8] dodecahedra, [HfO_6/ScO_6] octahedra, and [AlO_4] tetrahedra. Considering that Sc^{3+} and Cr^{3+} ions possess the same electrovalence and a similar radius, Cr^{3+} ions are more likely to replace Sc^{3+} ions in the octahedra (Sc^{3+} ($r_{[CN=6]}$ = 0.745 Å), Cr^{3+} ($r_{[CN=6]}$ = 0.615 Å)). To further understand the structure of YCHSA, we use the crystallographic data of $Ca_2GdZr_2Al_3O_{12}$ (COD-4338781) as the start model to refine the undoped YCHSA and YCHSA:0.08Cr^{3+},0.03Yb^{3+} samples, and the results are presented in Fig. S1 (ESI†) and Fig. 1c. The fitted parameters for the undoped YCHSA and YCHSA:0.08Cr^{3+},0.03Yb^{3+} samples were obtained as R_{wp} = 9.35%, R_p = 6.87% and R_{wp} = 9.68%, and R_p = 7.07%, respectively, which represent reliable refinement results. The detailed refined crystallographic and structure parameters are summarized in Tables S1 and S2 (ESI†). To further study the microstructure and elemental composition of YCHSA:Cr^{3+},Yb^{3+}, scanning electron microscopy (SEM) images and energy-dispersive X-ray spectrometry (EDS) patterns were recorded and are presented in Fig. 1d. The SEM image shows particles with an irregular shape and a size distribution range of 1–10 μm. The EDS mapping of randomly selected YCHSA:Cr^{3+},Yb^{3+} particle reveals that Y, Ca, Hf, Sc, Al, O, Cr, and Yb elements are uniformly distributed throughout the YCHSA:Cr^{3+},Yb^{3+} sample. The diffuse reflection spectra (DRS) of the undoped YCHSA, YCHSA:0.08Cr^{3+}, and YCHSA:0.08Cr^{3+},0.03Yb^{3+} samples were recorded and are shown in Fig. 2a. Compared with the DRS of undoped YCHSA, YCHSA:0.08Cr^{3+} and YCHSA:0.08Cr^{3+},0.03Yb^{3+} have two additional absorption bands distributed in the blue and red regions corresponding to the $^4A_{2g}$–$^4T_{1g}$ and $^4A_{2g}$–$^4T_{2g}$ transitions of the Cr^{3+} ions. The optical band gap of undoped YCHSA can be calculated by the following equations:[21]

$$F(R) = \frac{(1-R)^2}{2R} \tag{1}$$

$$(\alpha h\upsilon)^2 = A(h\upsilon - E_g) \tag{2}$$

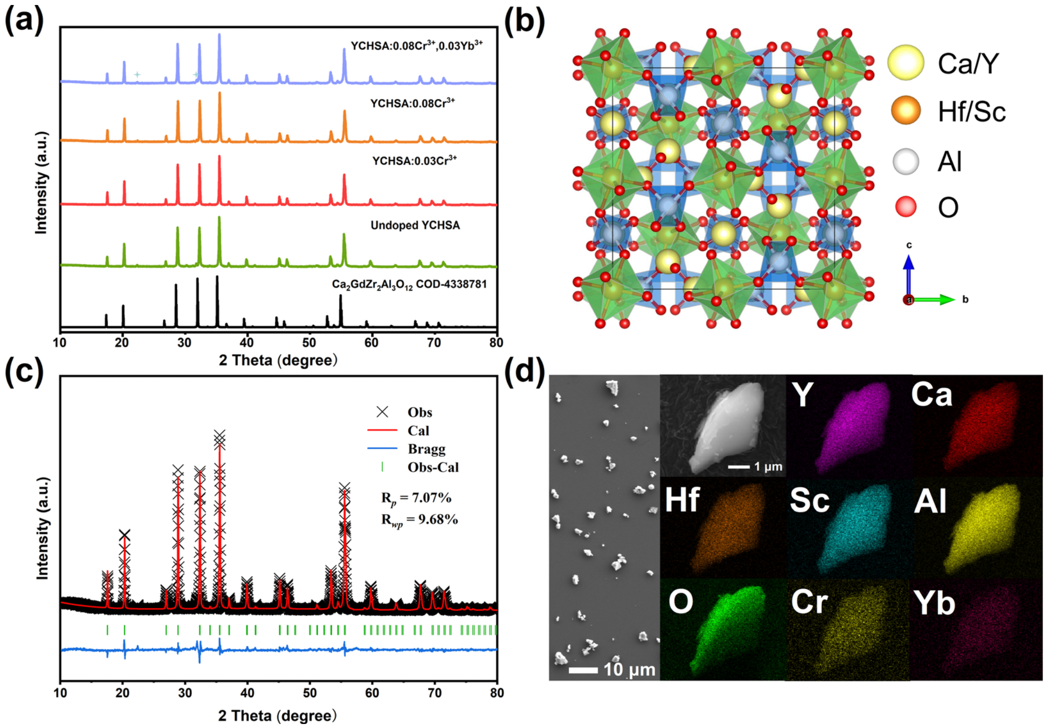

Fig. 1 (a) XRD patterns of the different doping concentrations of YCHSA:Cr^{3+},Yb^{3+}, and the diffraction peak data of $Ca_2GdZr_2Al_3O_{12}$. (b) Crystal structure of YCHSA. (c) Rietveld refinement XRD pattern of YCHSA:0.08Cr^{3+},0.03Yb^{3+}. (d) SEM image and EDS elemental mapping on a single particle of YCHSA:0.08Cr^{3+},0.03Yb^{3+}.

$$[h\upsilon F(R_\infty)]^2 = A(h\upsilon - E_g) \tag{3}$$

where R refers to the diffuse reflectance, $F(R)$ represents absorption, $h\upsilon$ denotes photon energy, and A and E_g are the absorption constant and band gap. On the basis of the above-mentioned formula, the band gap of undoped YCHSA was calculated to be 3.89 eV, as shown in Fig. 2b.

Luminescence properties

Fig. 3a shows the photoluminescence excitation (PLE) and photoluminescence (PL) spectra of the YCHSA:0.08Cr^{3+} phosphor. Two excitation bands at about 465 nm and 640 nm could be assigned to the $^4A_{2g} \rightarrow {}^4T_{1g}$ and $^4A_{2g} \rightarrow {}^4T_{2g}$ transitions of the Cr^{3+} ions. Under the excitation of 450 nm light, the PL spectrum shows a broadband NIR emission peaking at 757 nm with a FWHM of 110 nm, which corresponds to the $^4T_{2g} \rightarrow {}^4A_{2g}$ transition of the Cr^{3+} ions. According to Adachi's study, the local crystal-field parameters Dq, and B can be obtained by using the following formulas:[22]

$$\mathrm{Dq} = \frac{1}{10}E\left({}^4\mathrm{A}_{2g} \rightarrow {}^4\mathrm{T}_{2g}\right)_{\mathrm{ZPL}} = \frac{1}{10}\left({}^4\mathrm{T}_{2g}\right)_{\mathrm{ZPL}} \tag{4}$$

$$B = 6.18\mathrm{Dq} - \frac{1}{2}\left[(12.36\mathrm{Dq})^2 - 2.22E\left({}^2\mathrm{E}_g\right)_{\mathrm{ZPL}}\mathrm{Dq}\right]^{\frac{1}{2}} \tag{5}$$

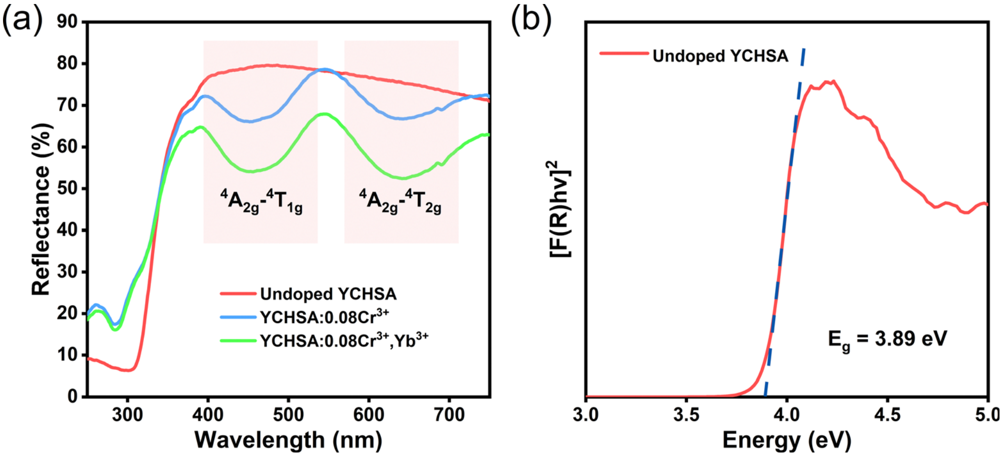

Fig. 2 (a) DRS of the undoped YCHSA, YCHSA:0.08Cr^{3+}, and YCHSA:0.08Cr^{3+},0.03Yb^{3+} samples. (b) Tucker curves of the undoped YCHSA.

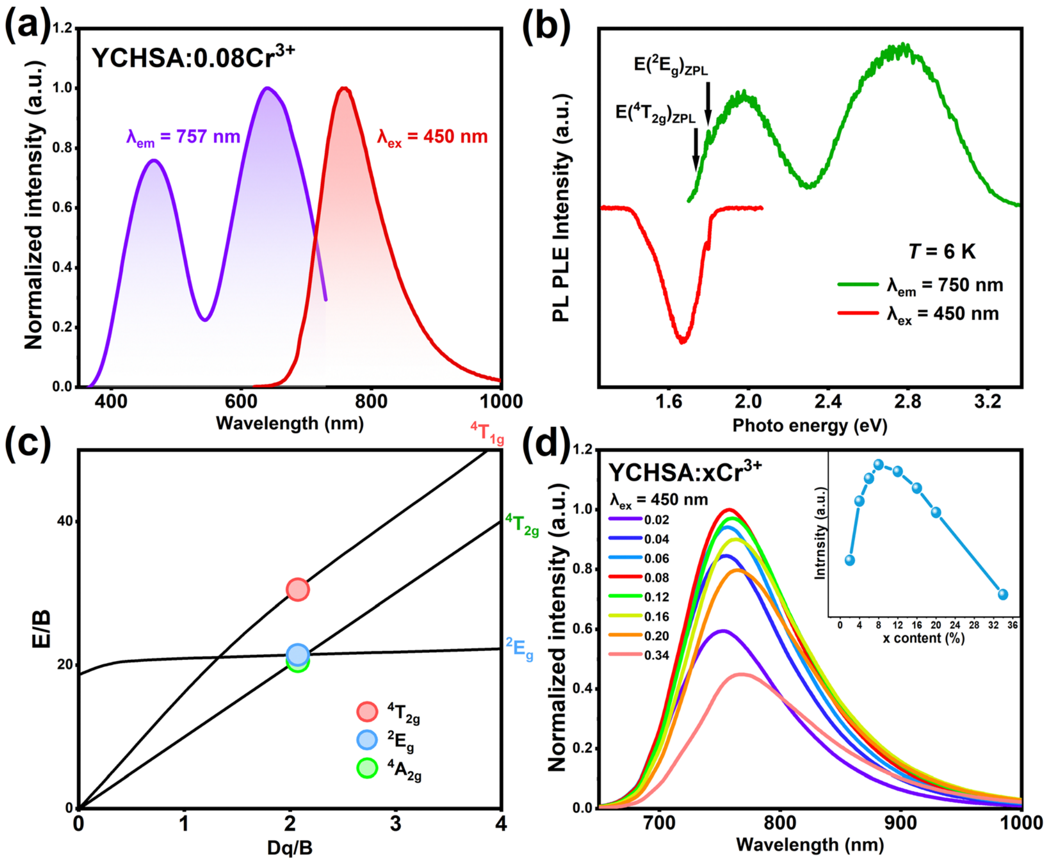

Fig. 3 (a) PL and PLE spectra of YCHSA:0.08Cr^{3+} at room temperature. (b) PL and PLE spectra of YCHSA:0.08Cr^{3+} when T = 6 K. (c) Tanabe–Sugano energy-level diagram for a $3d^3$ system in an octahedral crystal field. (d) Concentration-dependent emission spectra of YCHSA:$x$$Cr^{3+}$ (x = 0.02 to 0.34) phosphors. The upper inset shows the integrated emission intensity under different Cr^{3+} doping concentrations.

$$E(^4\mathrm{T}_{1\mathrm{g,a}})_{\mathrm{ZPL}} = 7.5B + 15\mathrm{Dq} - \frac{\mathrm{Dq}}{2}\left[\left(\frac{15B}{\mathrm{Dq}} + 10\right)^2 - \frac{480B}{\mathrm{Dq}}\right]^{\frac{1}{2}} \tag{6}$$

where Dq represents the crystal field intensity, B is the Racah parameter. The exact $E(^2\mathrm{E_g})_{\mathrm{ZPL}}$ energy position can be determined using the clear spike in the PLE spectrum at 6 K in Fig. 3b to be 1.79 eV. According to Adachi's previous study, $E(^4\mathrm{T_{2g}})_{\mathrm{ZPL}}$ is located near the onset of the PLE spectrum in Fig. 3b, where we take it as 1.73 eV. From eqn (4)–(6), Dq/B and $E(^4\mathrm{T_{1g}})_{\mathrm{ZPL}}$ can be calculated as 2.07 and 2.52 eV, respectively. According to the crystal field theory, Cr^{3+} ions reside in a weak crystal field with broadband NIR emission (corresponds to $^4\mathrm{T_{2g}} \rightarrow {^4\mathrm{A_{2g}}}$ transition). The values of $E(^4\mathrm{T_{1g}})_{\mathrm{ZPL}}/B$, $E(^4\mathrm{T_{2g}})_{\mathrm{ZPL}}/B$, and $E(^2\mathrm{E_g})_{\mathrm{ZPL}}/B$ are further calculated and represented by colored dots displayed in Fig. 3c. The symbol dots all show excellent agreement with the Tanabe–Sugano diagram curves, which represents reliable results.

Fig. 3d presents the PL spectra of YCHSA:$x$$Cr^{3+}$ (x = 0.02 to 0.34), with a maximum emission intensity of Cr^{3+} ions for x = 0.08. On further increasing the doping amount of Cr^{3+} ions, the emission intensity decreases due to the effect of concentration quenching. The critical energy transfer distance (R_c) can be calculated to understand the mechanism of the concentration quenching in YCHSA:Cr^{3+} by the following formula:[23]

$$R_{\mathrm{c}} = 2\left(\frac{3V}{4\pi x_{\mathrm{c}} N}\right)^{\frac{1}{3}} \tag{7}$$

where N is the number of center cations in a unit cell, V represents the cell volume, and x_c stands for the critical concentration. In YCHSA:Cr^{3+}, N = 8, V = 1902.11 Å^3 and x_c = 0.08. The calculated result of R_c is 17.84 Å. Therefore, the energy transfer mechanism among Cr^{3+} ions is governed by electric multipolar interactions since the exchange coupling takes place generally in a forbidden transition (the R_c is typically $<$ 5 Å). According to the report of Van Uitert, the PL intensity per activator concentration can be calculated by the following equation:[30]

$$\log\left(\frac{I}{x}\right) = -\frac{\theta}{3}\log x + A \tag{8}$$

where I represents the intensity of emission, x is the concentration of Cr^{3+} ions, and θ and A are constants under the same excitation. On the basis of the Dexter theory, the value of θ = 6, 8, and 10 correspond to the dipole–dipole (d–d), dipole–quadrupole (d–q), and quadrupole–quadrupole (q–q) interaction, respectively. Fig. S2 (ESI†) shows the dependence of $\log I/x$ and $\log x$; the slope ($-\theta/3$) of the line is calculated to be

−1.37, therefore the θ is 4.11 close to 6, indicating that the concentration quenching mechanism of Cr^{3+} ions in YCHSA is attributed to dipole–dipole (d–d) interaction. Fig. S3 (ESI†) shows a slight broadening of the NIR emission band and a red shift of the emission peak position as the concentration of Cr^{3+} ions increases. The former is due to the enhanced lattice distortion as the content of Cr^{3+} increases, leading to intensifying the splitting of the Cr^{3+} energy levels. The latter is attributed to the increased probability of the energy transfer from Cr^{3+} ions with higher $^4T_{2g}$ energy levels to Cr^{3+} ions with lower $^4T_{2g}$ energy levels by increasing the Cr^{3+}-concentration.

The PLE and PL spectra of YCHSA:0.08Cr^{3+} and YCHSA:0.08Cr^{3+},0.03Yb^{3+} are shown in Fig. 4a and b, respectively. It can be found that the PLE spectrum for monitoring the Yb^{3+} emission at 1032 nm is similar to the PLE spectrum for monitoring the Cr^{3+} emission at 757 nm. Moreover, under 450 nm excitation, the PL spectrum of YCHSA:0.08Cr^{3+},0.03Yb^{3+} contains not only the emission band of Cr^{3+} ions but also the emission lines of Yb^{3+} ions (corresponding to the $^2F_{5/2} \rightarrow {}^2F_{7/2}$ transition). These two features illustrate the occurrence of energy transfer from Cr^{3+} to Yb^{3+} ions. The PL spectra of YCHSA:0.08Cr^{3+},$y$$Yb^{3+}$ (y = 0.01 to 0.16) were recorded and are shown in Fig. 4c. As the concentration of Yb^{3+} ions increases, one can see the constantly enhanced emission intensity of Yb^{3+} ions and the emission intensity of the Cr^{3+} ions continuously decreases. Fig. 4d shows the FWHM and integrated emission intensity of YCHSA:Cr^{3+},$y$$Yb^{3+}$. When the concentration of Yb^{3+} ions increases, FWHM first increases to the maximum value (327 nm) for y = 0.03 and then decreases. Compared with some reported broadband NIR emission phosphors (Table 1), YCHSA:0.08Cr^{3+},0.03Yb^{3+} has a relatively broad emission band. The integrated emission intensity of the codoped samples decreases monotonically with an increase in the concentration of Yb^{3+} ions. As illustrated in Fig. S4 (ESI†), the internal quantum efficiency (IQE) of YCHSA:0.08Cr^{3+} and YCHSA:0.08Cr^{3+},0.03Yb^{3+} samples is measured and found to be 85.8% and 67.8%, respectively. A partial energy level diagram of electron transition in YCHSA:Cr^{3+},Yb^{3+} is given in Fig. 4e to understand the mechanism of energy transfer from the Cr^{3+} to Yb^{3+} ions. Under 450 nm excitation, the electrons of Cr^{3+} ions jump from the ground state $^4A_{2g}$ to the excited state and relax to the lowest excited state $^4T_{2g}$. Next, part of the electrons return to the ground state $^4A_{2g}$ with NIR emission covering from 650 to 900 nm. On part of the energy being transferred to the Yb^{3+} ions, electrons are excited from the $^2F_{7/2}$ to $^2F_{5/2}$ of the Yb^{3+} ions, and finally, return to $^2F_{7/2}$ with the emission around 1000 nm in the long wavelength region.

Fig. 4f presents the decay curves of YCHSA:0.08Cr^{3+},$y$$Yb^{3+}$ under 450 nm excitation and monitoring at 757 nm. The PL lifetime of Cr^{3+} ions at various values of y is calculated, and the detailed results are listed in Table S3 (ESI†). As the concentration of Yb^{3+} ions increases, the PL lifetime of Cr^{3+} ions decreases monotonically from 73.55 to 22.68 μs. The energy transfer efficiency from the Cr^{3+} to Yb^{3+} ions can be calculated by the following formula:[31]

$$\eta_{\mathrm{ET}} = 1 - \frac{\tau}{\tau_0} \tag{9}$$

where τ_0 and τ are the Cr^{3+} PL lifetime in the absence and the presence of Yb^{3+}, respectively. As shown in Fig. 4g and Table S4 (ESI†), the energy transfer efficiency increases continuously as the concentration of the Yb^{3+} ions increases and reaches 69.16% at y = 0.16, which is ascribed to the increasing probability of the energy transfer from the Cr^{3+} ions to the neighboring Yb^{3+} ions, indicating the enhanced rapidly energy transfer with an increase in the concentration of Yb^{3+} ions.

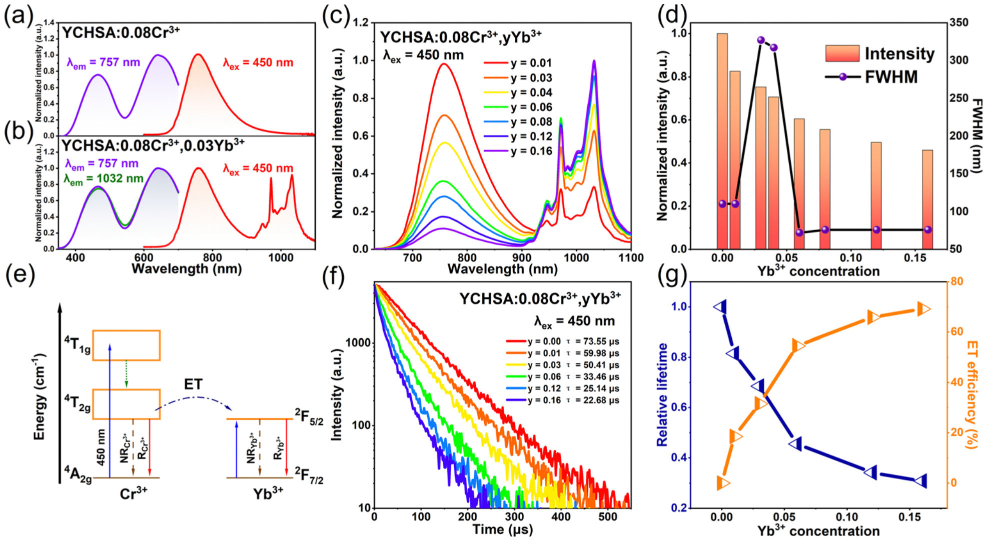

Fig. 4 (a) PLE and PL spectra of YCHSA:0.08Cr^{3+} and YCHSA:0.08Cr^{3+},0.03Yb^{3+}. (b) Concentration-dependent PL spectra of YCHSA:0.08Cr^{3+},$y$$Yb^{3+}$ (y = 0.01 to 0.16). (c) Emission integrated intensity and FWHM of YCHSA:0.08Cr^{3+},$y$$Yb^{3+}$. (d) Partial energy level diagram for the energy transfer process of YCHSA:Cr^{3+},Yb^{3+}. (e) PL decay curves of the YCHSA:0.08Cr^{3+},$y$$Yb^{3+}$ samples. (f) Relative PL lifetime of Cr^{3+} ions and (g) energy transfer efficiency in YCHSA:0.08Cr^{3+},$y$$Yb^{3+}$ samples.

Table 1 PL performance of some broadband NIR emission phosphors as well as photoelectric properties of the fabricated NIR pc-LEDs devices

Phosphor	FWHM (nm)	$I_{423K/303K}$ (%)	Photoelectric conversion efficiency (%)	Output power (mW)	Ref.
$Y_2CaHfScAl_3O_{12}$:0.08Cr^{3+},0.03Yb^{3+}	327	83	29.7	63.6 mW@100 mA	This work
$Lu_2CaMg_2Si_3O_{12}$:Cr^{3+}	125	70	14.8	59.5 mW@100 mA	24
$Ca_2LaHf_2Al_3O_{12}$:Cr^{3+}, Yb^{3+}	300	—	—	33.24 mW@200 mA	25
$Gd_3Sc_{1.5}Al_{0.5}Ga_3O_{12}$:$Cr^{3+}$,$Yb^{3+}$	—	97	24	50 mW@100 mA	26
La_2MgHfO_6:Cr^{3+},Yb^{3+}	333	81.6	3.7	—	27
$LiInSi_2O_6$:Cr^{3+}	143	77	17.2	51.6 mW@100 mA	13
$Ca_2LuHf_2Al_3O_{12}$:Cr^{3+}	—	—	21.28	46.09 mW@100 mA	28
$CaLu_2Mg_2Si_3O_{12}$:Cr^{3+}	128	82.3	11.6	34.75 mW@100 mA	29

Photoluminescence thermal stability

Photoluminescence thermal stability is a key characteristic for evaluating phosphors, as the operating temperature of LED devices is usually around 400 K. Fig. 5a, b and Fig. S5, S6 (ESI†) show the temperature-dependent PL spectra of YCHSA:0.08-Cr^{3+},$y$$Yb^{3+}$ (y = 0, 0.03, 0.09 and 0.22) varying from 303 to 483 K, respectively. Fig. 5c shows the temperature dependences of Cr^{3+}, Yb^{3+}, and the total emission intensity. Under the excitation of 450 nm, the Cr^{3+} ions show similar thermal quenching behaviour with the increasing temperature, and the Cr^{3+} ions emission intensity at 423 K is ∼76% of that at 303 K. However, the emissions of Yb^{3+} ions are enhanced with increasing temperature in the range of 303–423 K. Thus, the introduction of Yb^{3+} ions into YCHSA:0.08Cr^{3+} considerably improves the thermal stability of the YCHSA:0.08Cr^{3+},$y$$Yb^{3+}$. The total emission intensity of YCHSA:0.08Cr^{3+},$y$$Yb^{3+}$ (y = 0, 0.03, 0.09 and 0.22) increased from 76% for y = 0 to 96% for y = 0.22 at 423 K. YCHSA:0.08Cr^{3+},0.03Yb^{3+} retained 83% of the initial emission intensity when the temperature reached 423 K, indicating YCHSA:0.08Cr^{3+},0.03Yb^{3+} has better stability than most of the reported NIR phosphors (Table 1). The enhancement of thermal stability can be attributed to the results of rapid energy transfer between Cr^{3+}–Yb^{3+} ions pairs against thermal deactivation in Cr^{3+} ion emitting states.[32]

It can be seen from Fig. 5b that the Yb^{3+}-emission lines (located within 900–1100 nm) show different changes with the increase of temperature. The emission lines at 1032 and 1020 nm decrease rapidly, while the emission line at 949 nm is continuously enhanced. This phenomenon can be well explained by the Yb^{3+} ion energy level splitting. Due to the effect of the crystal field and the symmetry of the surrounding environment, the $^2F_{5/2}$ energy levels of the Yb^{3+} ions split into three Stark energy levels and the $^2F_{7/2}$ energy levels of Yb^{3+} ions split into four Stark energy levels in the YCHSA matrix as shown in Fig. 5d. The colored arrows in Fig. 5b correspond to the emission peaks marked with the same colors that can be directly identified in Fig. 5b. The black arrows correspond to emission peaks that cannot be directly identified in the spectrum, which are calculated from the determined energy levels. The emission lines at 910 nm, 937 nm, 952 nm, and 963 nm originate from the Stark level (2) of $^2F_{5/2}$ to the Stark levels of $^2F_{7/2}$ transition, The 949 nm, 982 nm, 996 nm, and 1007 nm emission lines are derived from the Stark level (1) of $^2F_{5/2}$ to the Stark levels of $^2F_{7/2}$ transition, The emission lines at 971 nm, 1001 nm, 1020 nm, and 1032 nm come from the Stark

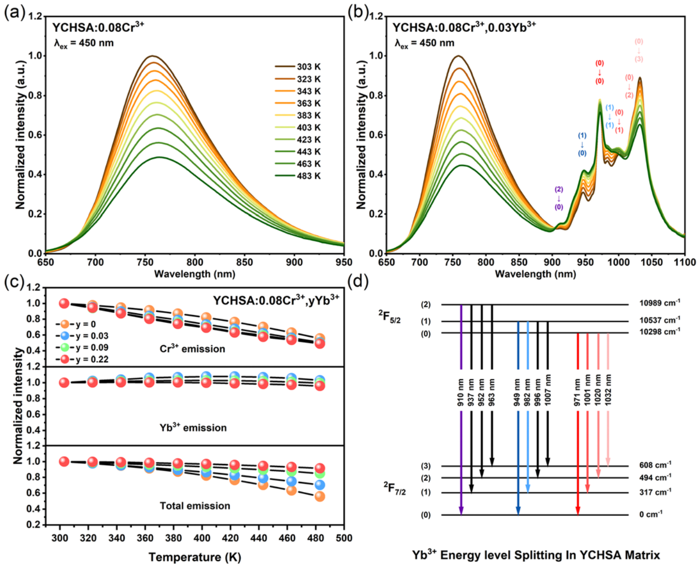

Fig. 5 Temperature-dependent normalized emission spectra of YCHSA:0.08Cr^{3+} (a) and YCHSA:0.08Cr^{3+},0.03Yb^{3+} (b), normalized integrated emission intensities of Cr^{3+}, Yb^{3+} ions and total emission in YCHSA:0.08Cr^{3+},$y$$Yb^{3+}$ (y = 0, 0.03, 0.09 and 0.22) with increasing temperature (c) and the energy level of the Yb^{3+} ions in the YCHSA matrix (d).

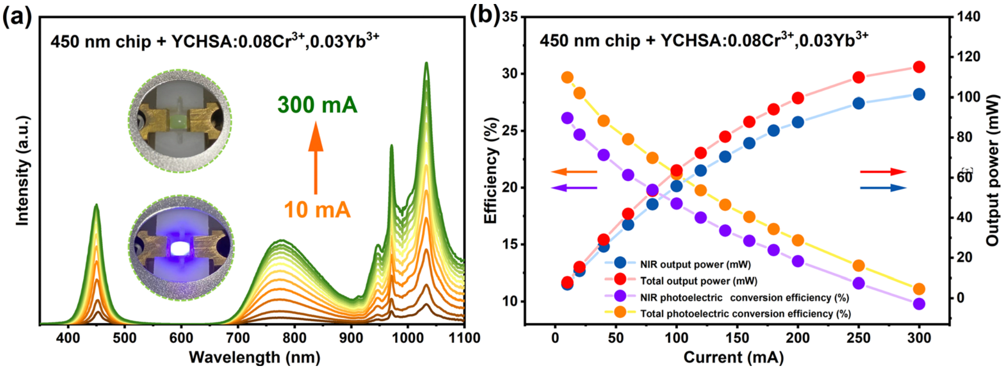

Fig. 6 (a) Luminescence spectra of the NIR pc-LED fabricated using YCHSA:0.08Cr^{3+},0.03Yb^{3+} under different drive currents. The inset pictures show that the fabricated pc-LED is off and on. (b) Output power and photoelectric conversion efficiency under various drive currents.

level (0) of $^2F_{5/2}$ to the Stark levels of $^2F_{7/2}$ transition. As the temperature increases, more electrons are thermally distributed to the higher Stark level of $^2F_{5/2}$, so the emission lines originating from the Stark levels (1) and (2) are enhanced and the emission lines coming from the lowest Stark level (0) are weakened.

Fabrication of NIR pc-LEDs

Given the superior photoluminescence properties of the YCHSA:Cr^{3+},Yb^{3+} phosphors, NIR pc-LEDs are fabricated by coating the samples (YCHSA:0.08Cr^{3+},0.03Yb^{3+}) on commercial InGaN chips (450 nm). Fig. 6a shows the luminescence spectra of the NIR pc-LED device obtained at different drive currents ranging from 10 to 300 mA. With an increase in the current, the spectral profile of the as-fabricated pc-LEDs has no changes except for the continuous intensity increase. The inset pictures of Fig. 6a are taken by a visible camera when the fabricated NIR pc-LED is off and on, respectively. From Fig. 6b the total output power and NIR output power gradually increase and reach 63.6 mW and 55.8 mW at 100 mA, while the total photoelectric conversion efficiency and NIR photoelectric conversion efficiency decrease gradually from 29.7% to 21.2% and 26.1% to 18.6% due to the efficiency of the blue LED chip decreasing. Detailed test information is listed in Table S5 (ESI†). The fabricated NIR pc-LEDs show excellent photoelectric properties compared with that of the previously reported broadband NIR emission phosphors in Table 1.

NIR pc-LEDs for applications

Since different inks have different absorption in NIR light, we exploited this property to explore the application of fabricated NIR pc-LEDs in information encryption. As shown in Fig. 7a, we first use carbon black ink to print important information on an A4 paper. Then we use a black water pen to draw black squares to obscure the important information. Under natural light, we can only see a black square. But when we light up the NIR pc-LED fabricated with YCHSA:0.08Cr^{3+},0.03Yb^{3+} and take pictures with a NIR camera, important information appears. We also explored the application of fabricated NIR pc-LEDs in non-invasive detection. As shown in Fig. 7b, it is hard to locate veins in the palm through a visible light camera under natural

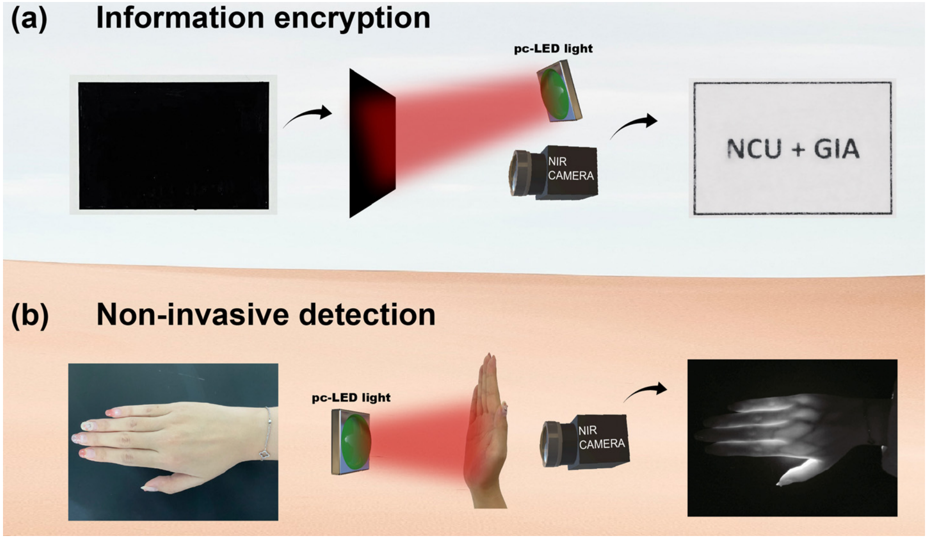

Fig. 7 Applications in information encryption (a) and non-invasive detection (b).

light, while it is easy to obtain a clear distribution of veins in the palm when we place the palm between the NIR pc-LED and the NIR camera and take a photo. These results reveal that YCHSA:Cr^{3+},Yb^{3+} have great potential for information encryption and non-invasive detection applications.

Conclusions

In summary, a series of efficient super broadband and thermally stable NIR phosphors have been developed by exploiting the YCHSA garnet as the host for Cr^{3+} and Yb^{3+} ions. Under 450 nm excitation, the YCHSA:0.08Cr^{3+} phosphors show a broad NIR emission peaking at 757 nm with a FWHM of 110 nm and good thermal stability ($I_{423K/303K}$ = 76%). On further introduction of Yb^{3+} ions, the YCHSA:0.08Cr^{3+},0.03Yb^{3+} has an emission band with a FWHM of 327 nm covering 700–1100 nm and enhanced thermal stability ($I_{423K/303K}$ = 83%). The high-performance NIR pc-LED device fabricated using the YCHSA:0.08Cr^{3+},0.03Yb^{3+} phosphor a and commercial blue chip produces 63.6 mW output power at 100 mA input current and its applications in information encryption and non-invasive detection are demonstrated. These results suggest that YCHSA:Cr^{3+},Yb^{3+} phosphors have great potential for spectroscopy applications.

Author contributions

Data curation: Pengcheng Luo; formal analysis: Dashuai Sun and Zeyu Lyu; investigation: Zheng Lu, Zhijun Li, Zhihang Yue, and Chengliang Lyu; methodology: Sida Shen; writing – original draft: Pengcheng Luo; writing – review & editing: Dashuai Sun, and Hongpeng You. All authors have read and agreed to the published version of the manuscript.

Conflicts of interest

The authors declare no conflicts of interest.

Acknowledgements

This work is financially supported by the Key Research Program of the Chinese Academy of Sciences (Grant No. ZDRW-CN-2021-3-3), the National Natural Science Foundation of China (Grant No. 52072363), and the Research Projects of Ganjiang Innovation Academy, Chinese Academy of Sciences (E255C001).

Notes and references

1 E. T. Basore, W. Xiao, X. Liu, J. Wu and J. Qiu, Broadband Near-Infrared Garnet Phosphors with Near-Unity Internal Quantum Efficiency, *Adv. Opt. Mater.*, 2020, **8**(12), 2000296.

2 Z. Zhou, N. Zhang, J. Chen, X. Zhou, M. S. Molokeev and C. Guo, The Vis-NIR multicolor emitting phosphor $Ba_4Gd_{3-}Na_3(PO_4)_6F_2$: Eu^{2+}, Pr^{3+} for LED towards plant growth, *J. Ind. Eng. Chem.*, 2018, **65**, 411–417.

3 D. Huang, H. Zhu, Z. Deng, H. Yang, J. Hu, S. Liang, D. Chen, E. Ma and W. Guo, A highly efficient and thermally stable broadband Cr^{3+}-activated double borate phosphor for near-infrared light-emitting diodes, *J. Mater. Chem. C*, 2021, **9**(1), 164–172.

4 V. Rajendran, M.-H. Fang, G. N. D. Guzman, T. Lesniewski, S. Mahlik, M. Grinberg, G. Leniec, S. M. Kaczmarek, Y.-S. Lin, K.-M. Lu, C.-M. Lin, H. Chang, S.-F. Hu and R.-S. Liu, Super Broadband Near-Infrared Phosphors with High Radiant Flux as Future Light Sources for Spectroscopy Applications, *ACS Energy Lett.*, 2018, **3**(11), 2679–2684.

5 D. Hayashi, A. M. van Dongen, J. Boerekamp, S. Spoor, G. Lucassen and J. Schleipen, A broadband LED source in visible to short-wave-infrared wavelengths for spectral tumor diagnostics, *Appl. Phys. Lett.*, 2017, **110**(23), 233701.

6 D. Wen, H. Liu, Y. Guo, Q. Zeng, M. Wu and R. S. Liu, Disorder-Order Conversion-Induced Enhancement of Thermal Stability of Pyroxene Near-Infrared Phosphors for Light-Emitting Diodes, *Angew. Chem., Int. Ed.*, 2022, **61**(28), e202204411.

7 Z. Wu, X. Han, Y. Zhou, K. Xing, S. Cao, L. Chen, R. Zeng, J. Zhao and B. Zou, Efficient broadband near-infrared luminescence of Cr^{3+} doped fluoride K_2NaInF_6 and its NIR-LED application toward veins imaging, *Chem. Eng. J.*, 2022, **427**, 131740.

8 E. Song, X. Jiang, Y. Zhou, Z. Lin, S. Ye, Z. Xia and Q. Zhang, Heavy Mn^{2+} Doped $MgAl_2O_4$ Phosphor for High-Efficient Near-Infrared Light-Emitting Diode and the Night-Vision Application, *Adv. Opt. Mater.*, 2019, **7**(24), 1901105.

9 Z. Tang, F. Du, H. Liu, Z. Leng, X. Sun, H. Xie, M. Que and Y. Wang, Eu^{2+}-Doped Layered Double Borate Phosphor with Ultrawide Near-Infrared Spectral Distribution in Response to Ultraviolet–Blue Light Excitation, *Adv. Opt. Mater.*, 2022, **10**(5), 2102204.

10 J. Qiao, G. Zhou, Y. Zhou, Q. Zhang and Z. Xia, Divalent europium-doped near-infrared-emitting phosphor for light-emitting diodes, *Nat. Commun.*, 2019, **10**(1), 5267, DOI: **10.1038/s41467-019-13293-0**.

11 X. Wang, F. Jahanbazi, J. Wei, C. U. Segre, W. Chen and Y. Mao, Charge Transfer-Triggered Bi^{3+} Near-Infrared Emission in $Y_2Ti_2O_7$ for Dual-Mode Temperature Sensing, *ACS Appl. Mater. Interfaces*, 2022, **14**(32), 36834–36844.

12 N. Mao, S. Liu, Z. Song, Y. Yu and Q. Liu, A broadband near-infrared phosphor $Ca_3Y_2Ge_3O_12$:Cr3+ with garnet structure, *J. Alloys Compd.*, 2021, **863**, 158699.

13 X. Xu, Q. Shao, L. Yao, Y. Dong and J. Jiang, Highly efficient and thermally stable Cr^{3+}-activated silicate phosphors for broadband near-infrared LED applications, *Chem. Eng. J.*, 2020, **383**, 123108.

14 C. Li and J. Zhong, Highly Efficient Broadband Near-Infrared Luminescence with Zero-Thermal-Quenching in Garnet $Y_3In_2Ga_3O_{12}$:Cr^{3+} Phosphors, *Chem. Mater.*, 2022, **34**(18), 8418–8426.

15 G. N. A. Guzman, V. Rajendran, Z. Bao, M. H. Fang, W. K. Pang, S. Mahlik, T. Lesniewski, M. Grinberg, M. S. Molokeev, G. Leniec, S. M. Kaczmarek, J. Ueda, K. M. Lu, S. F. Hu, H. Chang and R. S. Liu, Multi-Site Cation Control of Ultra-Broadband Near-

Infrared Phosphors for Application in Light-Emitting Diodes, *Inorg. Chem.*, 2020, **59**(20), 15101–15110.

16 H. Zeng, T. Zhou, L. Wang and R.-J. Xie, Two-Site Occupation for Exploring Ultra-Broadband Near-Infrared Phosphor-Double-Perovskite La_2MgZrO_6:Cr^3, *Chem. Mater.*, 2019, **31**(14), 5245–5253.

17 X. Zhou, J. Xiang, J. Zheng, X. Zhao, H. Suo and C. Guo, Ab initio two-sites occupancy and broadband near-infrared emission of Cr^{3+} in Li_2MgZrO_4, *Mater. Chem. Front.*, 2021, **5**(11), 4334–4342.

18 J. Xiang, J. Zheng, X. Zhao, X. Zhou, C. Chen, M. Jin and C. Guo, Synthesis of broadband NIR garnet phosphor $Ca_4ZrGe_3O_{12}$: Cr^{3+}, Yb^{3+} for NIR pc-LED applications, *Mater. Chem. Front.*, 2022, **6**(4), 440–449.

19 L. Yao, Q. Shao, S. Han, C. Liang, J. He and J. Jiang, Enhancing Near-Infrared Photoluminescence Intensity and Spectral Properties in Yb^{3+} Codoped $LiScP_2O_7$:Cr^{3+}, *Chem. Mater.*, 2020, **32**(6), 2430–2439.

20 M. U. Dumesso, W. Xiao, G. Zheng, E. T. Basore, M. Tang, X. Liu and J. Qiu, Efficient, Stable, and Ultra-Broadband Near-Infrared Garnet Phosphors for Miniaturized Optical Applications, *Adv. Opt. Mater.*, 2022, **10**(16), 2200676.

21 Y. Wang, Z. Wang, G. Wei, Y. Yang, S. He, J. Li, Y. Shi, R. Li, J. Zhang and P. Li, Ultra-Broadband and high efficiency Near-Infrared $Gd_3ZnGa_{5-2}GeO_{12}$:Cr^{3+} (x = 0–2.0) garnet phosphors via crystal field engineering, *Chem. Eng. J.*, 2022, **437**(1), 135346.

22 S. Adachi, Photoluminescence Spectroscopy and Crystal-Field Parameters of Cr^{3+} Ion in Red and Deep Red-Emitting Phosphors, *ECS J. Solid State Sci. Technol.*, 2019, **8**(12), R164–R168.

23 Z. Lu, D. Sun, Z. Lyu, S. Shen, L. Wang, J. Wang, H. Zhao and H. You, Novel efficient $SrMgY_3(SiO_4)_3F$:Ce^{3+},Tb^{3+} phosphor with tunable color and thermal stability through energy transfer, *J. Am. Ceram. Soc.*, 2022, **106**(2), 1182–1193.

24 W. Nie, L. Yao, G. Chen, S. Wu, Z. Liao, L. Han and X. Ye, A novel Cr^{3+}-doped $Lu_2CaMg_2Si_3O_{12}$ garnet phosphor with broadband emission for near-infrared applications, *Dalton Trans.*, 2021, **50**(24), 8446–8456.

25 D. Huang, Q. Ouyang, H. Xiao, B. Wang, H. Lian, Q. Zeng and J. Lin, Cr,Yb-codoped $Ca_2LaHf_2Al_3O_{12}$ garnet phosphor: electronic structure, broadband NIR emission and energy transfer properties, *Dalton Trans.*, 2021, **50**(3), 908–916.

26 E. T. Basore, H. Wu, W. Xiao, G. Zheng, X. Liu and J. Qiu, High-Power Broadband NIR LEDs Enabled by Highly Efficient Blue-to-NIR Conversion, *Adv. Opt. Mater.*, 2021, **9**(7), 2001660.

27 H. Suo, Y. Wang, X. Zhao, X. Zhang, L. Li, K. Guan, W. Ding, P. Li, Z. Wang and F. Wang, Rapid Nondestructive Detection Enabled by an Ultra-Broadband NIR pc-LED, *Laser Photonics Rev.*, 2022, **16**(7), 2200012.

28 L. Zhang, D. Wang, Z. Hao, X. Zhang, Gh Pan, H. Wu and J. Zhang, Cr^{3+}-Doped Broadband NIR Garnet Phosphor with Enhanced Luminescence and its Application in NIR Spectroscopy, *Adv. Opt. Mater.*, 2019, **7**(12), 1900185.

29 R. Li, Y. Liu, C. Yuan, G. Leniec, L. Miao, P. Sun, Z. Liu, Z. Luo, R. Dong and J. Jiang, Thermally Stable $CaLu_2Mg_2Si_3O_{12}$:Cr^{3+} Phosphors for NIR LEDs, *Adv. Opt. Mater.*, 2021, **9**(16), 2100388.

30 C. Zhong, L. Zhang, Y. Xu, X. Wu, S. Yin, X. Zhang and H. You, Novel broadband near-infrared emitting phosphor $LiGe_2(PO_4)3$:Cr^{3+} with tuning and enhancement of NIR emission by codoping Sb^{5+}, *J. Alloys Compd.*, 2022, **903**, 163945.

31 G. Liu, T. Hu, M. S. Molokeev and Z. Xia, Li/Na substitution and Yb^{3+} co-doping enabling tunable near-infrared emission in $LiIn_2SbO_6$:Cr^{3+} phosphors for light-emitting diodes, *iScience*, 2021, **24**(4), 102250.

32 S. He, L. Zhang, H. Wu, H. Wu, G. Pan, Z. Hao, X. Zhang, L. Zhang, H. Zhang and J. Zhang, Efficient Super Broadband NIR $Ca_2LuZr_2Al_3O_{12}$:Cr^{3+},Yb^{3+} Garnet Phosphor for pc-LED Light Source toward NIR Spectroscopy Applications, *Adv. Opt. Mater.*, 2020, **8**(6), 1901684.